

Cooperative Iron(II) Spin Crossover Complexes with N<sub>4</sub>O<sub>2</sub> Coordination SphereBirgit Weber,<sup>\*,†</sup> Eike Kaps,<sup>†</sup> Jan Weigand,<sup>†</sup> Chiara Carbonera,<sup>‡</sup> Jean-François Létard,<sup>\*,‡</sup> Klaus Achterhold,<sup>§</sup> and Fritz G. Parak<sup>§</sup>

Department of Chemistry and Biochemistry, Ludwig Maximilian University Munich, Butenandtstrasse 5-13 (Haus D), D-81377 München, Germany, Groupe des Sciences Moléculaires, Université Bordeaux I, ICMCB, CNRS, 87 Av. du Doc. A. Schweitzer, F-33608 Pessac, France, and Department of Physics, Technical University Munich, James-Franck-Strasse 85747 Garching, Germany

Received January 15, 2007

Two new spin crossover complexes [FeL(py)<sub>2</sub>] (**1**) and [FeL(DMAP)<sub>2</sub>] (**2**) with L being a tetradentate N<sub>2</sub>O<sub>2</sub><sup>2-</sup>-coordinating Schiff-base-like ligand [[([3,3']-[1,2-phenylenebis(iminomethylidene)])bis(2,4-pentanedionato)(2-)-N,N',O<sup>2</sup>,O<sup>2</sup>], py = pyridine and DMAP = *p*-dimethylaminopyridine have been investigated using temperature-dependent susceptibility and thermogravimetric and photomagnetic measurements as well as Mössbauer spectroscopy and X-ray structure analysis. Both complexes show a cooperative spin transition with an approximately 9 K wide thermal hysteresis loop in the case of **2** ( $T_{1/2\uparrow}$  = 183 K and  $T_{1/2\downarrow}$  = 174 K) and an approximately 2 K wide thermal hysteresis loop in the case of the pyridine diadduct **1** ( $T_{1/2\uparrow}$  = 191 K and  $T_{1/2\downarrow}$  = 189 K). The spin transition was additionally followed by different temperature-scanning calorimetry and Mössbauer spectroscopy for **2**, and a good agreement for the transition temperatures obtained with the different methods was found. Results from X-ray structure analysis indicate that the cooperative interactions are due to elastic interactions in both compounds. They are more pronounced in the case of **2** with very short intermolecular iron–iron distances of 7.2 Å and several intense C–C contacts. The change of the spin state at the iron center is accompanied by a change of the O–Fe–O angle, the so-called bit of the equatorial ligand, from 108° in the high-spin state to 90° in the low-spin state. The reflectivity measurements of both compounds give at low temperature indication that at the sample surface the light-induced excited spin state trapping (LIESST) effect occurs. In bulk condition using a SQUID magnetometer the complex **2** displays some photomagnetic properties with a photoexcitation level of 60% and a  $T(\text{LIESST})$  value of 53 K.

## 1. Introduction

Spin crossover complexes are an interesting class of switchable molecules<sup>1</sup> with possible future applications as molecular switches or in data storage devices.<sup>2</sup> As part of a more general program that deals with the purposeful synthesis of oligonuclear complexes with tuneable magnetic properties we investigated the properties of mononuclear iron(II) complexes with an octahedral N<sub>4</sub>O<sub>2</sub> coordination sphere as possible building blocks for larger systems. Although spin crossover could be observed for any octahedral

complex with d<sup>n</sup> ( $n = 4-7$ ) electron configuration, the spin transition in octahedral iron(II) complexes is by far the most thoroughly investigated with the diamagnetic low-spin (LS)

- (1) (a) Goodwin, H. A. *Coord. Chem. Rev.* **1976**, *18*, 293. (b) Gütllich, P. *Struct. Bonding (Berlin)* **1981**, *44*, 83. (c) König, E. *Prog. Inorg. Chem.* **1987**, *35*, 527. (d) Gütllich, P.; Hauser, A. *Coord. Chem. Rev.* **1990**, *97*, 1. (e) König, E. *Struct. Bonding (Berlin)* **1991**, *76*, 51. (f) Gütllich, P.; Hauser, A.; Spiering, H. *Angew. Chem., Int. Ed. Engl.* **1994**, *33*, 2024 and references therein. (g) Coronado, E.; Delhaes, P.; Gatteschi, D.; Müller, J. S. NATO ASI Series E; Kluwer Academic Publishing, 1996; Vol. 321, p 327. (h) Gütllich, P., Goodwin, H. A., Eds. *Spin Crossover in Transition Metal Compounds I–III*; Topics in Current Chemistry; Springer-Verlag: Berlin, Heidelberg, New York, 2004.
- (2) (a) Kahn, O.; Jay Martínez, C. *Science* **1998**, *279*, 44–48. (b) Kahn, O.; Jay, C.; Kröber, J.; Claude, R.; Grolière, F. Patent EP0666561, 1995. (c) Létard, J.-F.; Nguyen, O.; Daro, N. Patent FR0512476, 2005. (d) Létard, J.-F.; Guionneau, P.; Goux-Capes, L. *Spin Crossover in Transition Metals III*; Gütllich, P., Goodwin, H. A., Eds.; Topics in Current Chemistry; Springer: Wien, New York, 2004; Vol. 235, p 221.

\* To whom correspondence should be addressed. E-mail: bwmch@cup.uni-muenchen.de. (B.W.), letard@icmcb-bordeaux.cnrs.fr (J.-F.L.). Phone: +49-8921807772 (B.W.). Fax: +49-89218077407(B.W.).

<sup>†</sup> Ludwig Maximilian University Munich.

<sup>‡</sup> Université Bordeaux I.

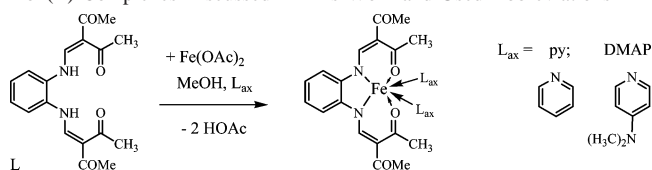
<sup>§</sup> Technical University Munich.

state and the paramagnetic high-spin (HS) state. Of those complexes investigated, about 90% exhibit an  $N_6$  coordination sphere.<sup>1</sup> Other examples with an  $N_4O_2^{3-5}$  or  $N_4S_2^6$  coordination sphere are seldom. In contrast to this observation, there are several examples for iron(III) spin crossover complexes with  $N_4O_2$  coordination sphere.<sup>1</sup>

The influence of chemical parameters such as the ligand, counterions, or solvent molecules on the spin transition, especially the transition temperature,  $T_{1/2}$ , is well understood by now. This is not the case for cooperative effects between the molecules during spin crossover phenomenon. The possibility to predict which effect is induced by a change of the ligand structure or other parameters is limited. Rigid linkers that allow communication between spin transition centers are often quoted to be necessary for the observation of this phenomenon. The most frequently used method is the application of suitable bridging ligands as covalent linkers between the metal centers.<sup>7</sup> However, here the question arises whether the observed properties are due to the covalent bridge or due to additional elastic interactions between the covalently linked units.<sup>8</sup> One possibility of elastic interactions is a communicating network of hydrogen bonds. Systematic investigations on iron(II) complexes with a dianionic  $N_4O_2$  salene-type Schiff base ligand did demonstrate that the properties of spin crossover are closely related to intermolecular interactions and crystal packing. Stepwise transitions, thermal hysteresis, or gradual spin crossover (SCO) were associated with small differences in the formation of infinite, hydrogen-bond-bridged chains.<sup>3-5</sup>  $\pi$ -Stacking or van der Waals interactions are rarely, however, strong intermolecular  $\pi$ - $\pi$  interactions due to extended aromatic rings that can enhance the cooperativity in iron(II) SCO complexes significantly.<sup>9</sup>

In this work we introduce two new  $N_4O_2$ -coordinated SCO complexes with cooperative spin transitions due to van der Waals interactions. Scheme 1 displays the general formula of the ligands and complexes used in this work. Complexes of these types of Schiff-base-like equatorial ligands were first investigated by Jäger.<sup>10</sup> A pentacoordinated iron(III) complex with nitric oxide as axial ligand was reported to show a gradual spin transition,<sup>11,12</sup> and two similar iron(II) complexes

**Scheme 1.** General Procedure for the Synthesis of the Octahedral Iron(II) Complexes Discussed in This Work and Used Abbreviations



with pyridine and imidazole, respectively, as axial ligands also perform temperature-dependent spin transitions.<sup>10,13</sup> In this work we use next to pyridine the sterically more demanding DMAP as axial ligands.

## 2. Experimental Section

**2.1. Syntheses.** If not described differently, all syntheses were carried out under argon using Schlenk tube techniques. All solvents were purified as described in the literature<sup>14</sup> and distilled under argon. The synthesis of the ligand  $H_2L$ <sup>15</sup> and iron(II) acetate<sup>16</sup> is described in literature. The complexes were prepared by conversion of the equatorial ligand with iron(II) acetate in the presence of an excess of the axial ligand in methanol (see Scheme 1). The composition of the complex was confirmed by elemental analysis in combination with thermogravimetric analysis.

**[FeL(py)<sub>2</sub>] (1)** ([3,3']-[1,2-phenylenebis(iminomethylidene)]bis(2,4-pentanedionato)(2-)- $N,N',O^2,O^2$ ]iron(II)·2pyridine: Iron(II) acetate (0.5 g, 2.10 mmol) and  $H_2L$  (0.41 g, 1.24 mmol) were dissolved in 10 mL of pyridine and 20 mL of methanol and refluxed for 0.5 h. After cooling, 2 mL of oxygen-free water was added to the solution and one-third of the solvent was removed by cold distillation. A further 5 mL of oxygen-free water was added to the solution to enable the slow crystallization of the product. The precipitate was filtered off and washed with a small amount of methanol. Yield: 0.48 g (72%). Anal. Calcd for  $C_{18}H_{18}N_2O_4Fe \cdot 2C_5H_5N$ : C, 62.23; H, 5.22; N, 10.37. Found: C, 61.15; H, 5.11; N, 10.02. IR (Nujol):  $\nu(CO) = 1634 \text{ cm}^{-1}$ . MS (DEI): base peak: 79  $m/z$  (pyridine; 100%); 382  $m/z$  ( $M^+$ , 6%). DTG: up to 170 °C, -14.1% = loss of 1 Py (theory, 14.6%); up to 250 °C, -28.2% = loss of 2 Py (theory, 29.3%); at 340 °C, decomposition.

**[FeL(DMAP)<sub>2</sub>] (2)** ([3,3']-[1,2-phenylenebis(iminomethylidene)]bis(2,4-pentanedionato)(2-)- $N,N',O^2,O^2$ ]iron(II)·2 $p$ -dimethylamino pyridine: This given compound can be first obtained by converting [FeL(MeOH)<sub>2</sub>] with DMAP in methanol. Another strategy consists of dissolving iron(II) acetate (0.63 g, 2.65 mmol),  $H_2L$  (0.51 g, 1.55 mmol), and DMAP (15 g, 0.123 mol) in 30 mL of methanol and refluxing for 0.5 h. After cooling, the fine crystalline product was filtered off, washed with a small amount of methanol, and dried in vacuum. Yield: 0.89 g (92%). Anal. Calcd for  $C_{18}H_{18}N_2O_4Fe \cdot 2C_7H_{10}N_2$ : C, 61.34; H, 6.11; N, 13.41. Found: C, 61.04; H, 6.26; N, 13.39. IR (Nujol):  $\nu(CO) = 1638 \text{ cm}^{-1}$ . MS (DEI): base peak: 121  $m/z$  (DMAP; 100%); 382  $m/z$  ( $M^+$ , 5%). DTG: up to 150 °C, -4.5% = loss of DMAP in the crystal; up to 250 °C, -26.5% = loss of 1 DMAP (theory, 19.5%); at 260 °C, decomposition.

- (3) Psomas, G.; Bréfuel, N.; Dahan, F.; Tuchagues, J.-P. *Inorg. Chem.* **2004**, *43*, 4590–4594.  
 (4) Boinnard, D.; Bousseksou, A.; Dworkin, A.; Savariault, J.-M.; Varret, F.; Tuchagues, J.-P. *Inorg. Chem.* **1994**, *33*, 271–281.  
 (5) Salmon, L.; Bousseksou, A.; Donnadieu, B.; Tuchagues, J.-P. *Inorg. Chem.* **2005**, *44*, 1763–1773.  
 (6) Grillo, V. A.; Gahan, L. R.; Hanson, G. R.; Stranger, R.; Hambley, T. W.; Murray, K. S.; Moubarak, B.; Cashion, J. D. *J. Chem. Soc., Dalton Trans.* **1998**, 2341–2348.  
 (7) (a) Real, J. A.; Gaspar, A. B.; Niel, V.; Munoz, M. C. *Coord. Chem. Rev.* **2003**, *236*, 121–141. (b) Niel, V.; Thompson, A. L.; Munoz, M. C.; Galet, A.; Goeta, A. E.; Real, J. A. *Angew. Chem., Int. Ed.* **2003**, *42*, 3760–3763.  
 (8) Weber, B.; Tandon, R.; Himsl, D. Z. *Anorg. Allg. Chem.* **2007**, *633*, 1159–1162.  
 (9) (a) Létard, J.-F.; Guionneau, P.; Codjovi, E.; Lavastre, O.; Bravic, G.; Chasseau, D.; Kahn, O. *J. Am. Chem. Soc.* **1997**, *119*, 10861. (b) Zhong, J. Z.; Tao, J.-Q.; Yu, Z.; Dun, C.-Y.; Liu, Y.-J.; You, X.-Z. *J. Chem. Soc., Dalton Trans.* **1998**, 327–328.  
 (10) Jäger, E.-G. *Chemistry at the Beginning of the Third Millennium*; Fabbri, L., Poggi, A., Eds.; Springer-Verlag: Berlin, 2000; pp 103–138.

- (11) Numata, Y.; Kubokura, K.; Nonaka, Y.; Okawa, H.; Kida, S. *Inorg. Chim. Acta* **1980**, *43*, 193–197.  
 (12) König, E.; Ritter, G.; Dengler, J.; Larkworthy, L. F. *Inorg. Chem.* **1992**, *31*, 1196–1202.  
 (13) (a) Leibel, G. Ph.D. Thesis, University of Jena, Jena, Germany, 2003. (b) Müller, B. R.; Leibel, G.; Jäger, E.-G. *Chem. Phys. Lett.* **2000**, *319*, 368–374.  
 (14) Autorenkollektiv. *Organikum*; Johann Ambrosius Barth Verlagsgesellschaft mbH, Leipzig, 1993.  
 (15) Wolf, L.; Jäger, E.-G. *Z. Anorg. Allg. Chem.* **1966**, *346*, 76.  
 (16) Heyn, B.; Hipler, B.; Kreisel, G.; Schreer, H.; Walter, D. *Anorganische Synthesechemie*; Springer-Verlag: Heidelberg, Germany, 1986.

**2.2. Physical Measurements.** Magnetic measurements of pulverized samples were performed on a Quantum Design MPMSR-XL SQUID magnetometer in a temperature range from 2 to 300 K. All measurements were carried out at two field strengths (0.2 and 0.5 T) in the settle mode (average scan rate 0.3 K/min). The data were corrected for the magnetization of the sample holder, and diamagnetic corrections were made using estimated values from Pascal's constants. Thermogravimetric analysis was performed on an electromagnetic-compensated thermobalance (own construction FSU Jena, Germany) with a heating rate of around 10 K/min. Elemental analysis was performed on an Elementar Vario EL instrument.

Thermoanalytical measurements between room temperature and  $-100$  °C were recorded and analyzed on a Setaram DSC 141 including a home-made low-temperature attachment. The instrument was calibrated at solid  $CCl_4$  transition and melting temperatures. The differential scanning calorimetry (DSC) charts were recorded at the temperature-scanning rate of 1 °C/min. The cooling and heating charts of the DSC measurements were repeated three times and have been summed to obtain the average DSC curve. The freezing temperature was determined by the crossing point of the linear rising part of the peak and the average background. The enthalpy of freezing was obtained from the peak area and used for the energy calibration. The melting temperature was determined using the dropping linear part of the peak.

Mössbauer spectra have been recorded using a conventional Mössbauer spectrometer operating in the constant acceleration mode. The sample was placed in an Oxford bath cryostat.

For the light-induced excited spin state trapping (LIESST) measurements, the measurements of the diffuse absorption spectra and reflectivity signal were performed by using a custom-built setup equipped with an SM240 spectrometer (Opton Laser International). This equipment allows us to record both the diffuse absorption spectra within the range of 500–900 nm at a given temperature and the temperature dependence (5–290 K) of the reflectivity signal at a selected wavelength ( $\pm 2.5$  nm). The diffuse reflectance spectrum was calibrated with respect to charcoal activated (Merck) as black standard and barium sulfate ( $BaSO_4$ , Din 5033, Merck) as white standard.

The photomagnetic measurements were performed using a Spectra Physics series 2025 Kr<sup>+</sup> laser (530.9, 647.1–676.4, 752.5–799.3 nm) or a diode laser ( $\lambda = 830$  nm) coupled via an optical fiber to the cavity of the MPMS-55 Quantum Design SQUID magnetometer operating with an external magnetic field of 2 T within the 2–300 K temperature range and a speed of 10 K min<sup>-1</sup> in the settle mode at atmospheric pressure.<sup>17</sup> The power of the laser beam on the sample whatever the selected wavelength(s) used was adjusted to 5 mW cm<sup>-2</sup>. Bulk attenuation of light intensity was limited as much as possible by the preparation of a thin layer of compound. It is noteworthy that there was no change in the data due to sample heating upon laser irradiation. The weight of these thin layer samples—approximately 0.2 mg—was obtained by comparison of the measured thermal SCO curve with another curve of a more accurately weighed sample of the same compound. The data were corrected for the magnetization of the sample holder and for diamagnetic contributions, estimated from Pascal's constants.

**2.3. Crystal Structure Determinations.** The intensity data were collected on a Stoe IPDS diffractometer using graphite-monochro-

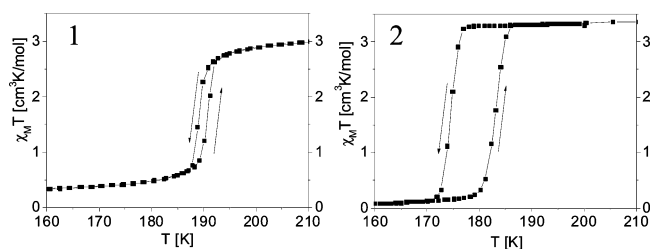


**Figure 1.** Thermal dependence of  $\chi_M T$  for **1** and **2**.

ated Mo K $\alpha$  radiation. Data were corrected for Lorentz and polarization effect and for absorption (XRed).<sup>18</sup> The structures were solved by direct methods (Sir 97<sup>19</sup>) and refined by full-matrix least-squares techniques against  $F_0^2$  (SHELXL-97<sup>20</sup>). The hydrogen atoms were included at calculated positions with fixed thermal parameters. All non-hydrogen atoms were refined anisotropically. ORTEP-III was used for structure representation.<sup>21</sup>

### 3. Results

**3.1. Magnetic Properties, Heat Capacity Measurements, and Mössbauer Spectroscopy.** Figure 1 shows the thermal dependence of the  $\chi_M T$  product ( $\chi_M =$  molar susceptibility) for  $[FeL(py)_2]$  (**1**) and  $[FeL(DMAP)_2]$  (**2**) obtained in the settle mode. At room temperature, the  $\chi_M T$  values of **1** and **2** (i.e., respectively, 3.32 and 3.25 cm<sup>3</sup> K mol<sup>-1</sup>) are within the region expected for a HS iron(II). As the temperature is lowered, a cooperative transition into the LS state takes place in both cases. An approximately 9 K wide hysteresis is observed for **2** with a characteristic temperature  $T_{1/2c}$  of 174 K (estimated on cooling at HS molar fraction,  $\gamma_{HS}$ , equal to 0.5) and  $T_{1/2h}$  of 183 K for heating up. In the case of **1** a small, approximately 2 K, wide hysteresis with  $T_{1/2c} = 189$  K and  $T_{1/2h} = 191$  K is observed. For both complexes, hysteresis loops can be repeated several times.

Differential scanning calorimetry measurements were recorded between room temperature and 165 K for both SCO complexes with a heating and cooling rate of 1 K/min. The experimental curves of the heating rate versus  $T$  for both complexes are given in Supporting Information, Figure S1. The values of the transition temperatures from the onset of the DSC peaks are with 190.4/194.8 K (cooling/heating) for **1** and 176.8/186.5 K (cooling/heating) for **2**, in good agreement with results from the susceptibility measurements, taking into account that the onset temperatures were determined with a scanning rate a little bit faster than for the SQUID in the settle mode (see Table 1). The enthalpy changes,  $\Delta H$ , associated with each step of the spin conversion have been calculated by averaging the measurements obtained from increasing and decreasing temperatures. The average values are  $7.30 \pm 0.14$  kJ mol<sup>-1</sup> for **1** and  $5.72 \pm 0.12$  kJ mol<sup>-1</sup> for **2**. From the mean values ( $T_{cooling}$

(17) (a) Létard, J. F.; Guionneau, P.; Rabardel, L.; Howard, J. A. K.; Goeta, A. E.; Chasseau, D.; Kahn, O. *Inorg. Chem.* **1998**, *37*, 4432–4441. (b) Létard, J. F.; Chastanet, G.; Nguyen, O.; Marcen, S.; Marchivie, M.; Guionneau, P.; Chasseau, D.; Gutlich, P. *Monatsh. Chem.* **2003**, *134*, 165–182. (c) Létard, J.-F. *J. Mater. Chem.* **2006**, *16*, 2550.

(18) Sheldrick, G. M. *SHELXL97*; University of Göttingen: Göttingen, Germany, 1993.

(19) Altomare, A.; Burla, M. C.; Camalli, G. M.; Cascarano, G.; Giacovazzo, C.; Guagliardi, A.; Moliterni, A. G. G.; Polidori, G.; Spagna, R. *J. Appl. Crystallogr.* **1999**, *32*, 115–119.

(20) Sheldrick, G. M. *Acta Crystallogr., Sect. A* **1990**, *46*, 467–473.

(21) (a) Johnson, C. K.; Burnett, M. N. *ORTEP-III*; Oak-Ridge National Laboratory: Oak-Ridge, TN, 1996. (b) Farrugia, L. J. *J. Appl. Crystallogr.* **1997**, *30*, 565.

**Table 1.** Influence of the Scanning Rate on the Spin Transition Behavior of [FeL(py)<sub>2</sub>] and [FeL(DMAP)<sub>2</sub>]

compd	rate [K/min]	$T_{1/2}^{\downarrow}$ [K]	$T_{1/2}^{\uparrow}$ (heating) [K]	$\Delta T$ [K]
[FeL(py) <sub>2</sub> ]	0.3 <sup>a</sup>	189	191	2
	1 <sup>b</sup>	190.4	194.8	4
[FeL(DMAP) <sub>2</sub> ]	0.3 <sup>a</sup>	174	183	9
	1 <sup>b</sup>	176.8	186.5	10
	settle <sup>c</sup>	173	180	7

<sup>a</sup> SQUID measurements, in the settle mode the data points were taken in 1 K steps leading to an average rate of 0.3 K/min;  $\gamma_{\text{HS}} = 0.5$ . <sup>b</sup> DSC measurements, onset temperature. <sup>c</sup> Mössbauer measurements.

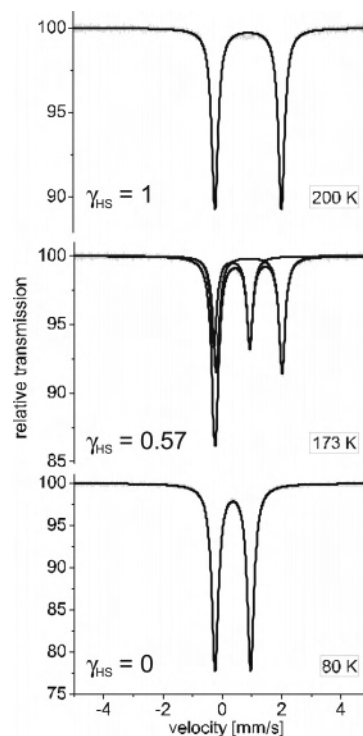
+  $T_{\text{heating}}/2$ , the entropy changes,  $\Delta S$ , values of  $37.8 \pm 1.10$  J mol<sup>-1</sup> K<sup>-1</sup> for **1** and  $31.5 \pm 0.84$  J mol<sup>-1</sup> K<sup>-1</sup> for **2** were calculated.

Knowing the  $\Delta H$  and  $\Delta S$  values the intermolecular interaction parameter  $\Gamma$  can be determined using the mean-field model proposed by Slichter and Drickamer (eq 1<sup>22</sup>).

$$\Delta G_{\text{HL}} = \Delta H_{\text{HL}} - T\Delta S_{\text{HL}} + \Gamma(1 - 2\gamma_{\text{HS}}) \quad (1)$$

This was done by least-squares fittings of the  $\gamma_{\text{HS}}$  (HS molar fraction) versus  $T$  curves of the two complexes with  $\Delta H$  and  $\Delta S$  as fixed parameters. In Supporting Information, Figure S2, the fit of  $\gamma_{\text{HS}}$  versus  $T$  is represented for the two complexes. The obtained parameters are, respectively,  $\Gamma = 3.40 \pm 0.08$  kJ mol<sup>-1</sup> and  $\Gamma = 3.78 \pm 0.41$  kJ mol<sup>-1</sup> for **1** and **2**. Following the suggestion of Purcell and Edwards<sup>23</sup> the parameter  $C$  ( $= \Gamma/2RT_{1/2}$  = cooperativity factor) was determined. Its value is, respectively, 1.08 and 1.28 for **1** and **2**. The cooperativity factor is above unity for both complexes in agreement with the existence of a thermal hysteresis loop. Furthermore it increases from **1** to **2** reflecting the increasing width of the thermal hysteresis.

The spin transition of **2** was also followed using Mössbauer spectroscopy in the temperature region of 80–200 K in the heating and cooling mode. Selected spectra at different temperatures followed in the cooling mode are given in Figure 2 with the HS mole fraction indicated. Values of the Mössbauer parameters obtained by least-squares fitting of the spectra are gathered in Supporting Information, Table S1. At 200 K the Mössbauer spectrum consists of a unique quadrupole-split doublet, with an isomer shift of 0.99 mm/s and a quadrupole splitting of 2.24 mm/s. These parameters are typical for HS iron(II). Below 170 K a LS iron(II) doublet appears with the parameters  $\delta = 0.47$  mm/s and  $\Delta E_{\text{Q}} = 1.20$  mm/s at 80 K. No evidence of residual LS and HS fractions are found in the high-temperature ( $T > 185$  K) and low-temperature ( $T < 165$  K) spectra, respectively. The high-spin mole fraction  $\gamma_{\text{HS}}$  at each temperature was deduced from the area ratio  $A_{\text{HS}}/A_{\text{tot}}$  determined from the least-squares fitting of the spectra ( $A_{\text{HS}}$  = area of the HS doublet;  $A_{\text{tot}}$  = total Mössbauer absorption). The transition temperatures,  $T_{1/2^{\downarrow}} = 173$  K and  $T_{1/2^{\uparrow}} = 180$  K, are in good agreement with the results from the other methods (see Table 1). For compound **1**, the Mössbauer parameters were determined for the HS and the LS form. They are  $\delta = 0.45$  mm/s,  $\Delta E_{\text{Q}} = 1.32$

**Figure 2.** Plot of the Mössbauer spectra of **2** at 80, 173, and 200 K with the high-spin molar fraction indicated.

mm/s at 180 K and  $\delta = 0.97$  mm/s,  $\Delta E_{\text{Q}} = 2.17$  mm/s at 200 K (LS and HS form, respectively, see Supporting Information, Table S2).

**3.2. X-ray Structure Analysis.** Crystals suitable for X-ray structure analysis have been obtained for both complexes. Selected bond lengths and angles within the first coordination sphere are summarized in Table 2. The crystallographic data of the complexes are summarized in Table 3. Ortep drawings of the HS forms of **1** and **2** are given in Figures 3 and 4. In the case of **1**, the X-ray structure was measured before and after the spin transition. For **2** the determination of the X-ray structure was possible only for the HS state because the crystals crumble while cooling down (possibly due to a phase transition).

The average bond lengths in the HS state are 2.08 (Fe–N<sub>eq</sub>), 2.01 (Fe–O<sub>eq</sub>), and 2.25 Å (Fe–N<sub>ax</sub>). Upon spin transition a shortening of the bond lengths of about 10% as discussed for other iron(II) SCO complexes in literature<sup>24</sup> is observed. The variation is more pronounced for the axial ligands ( $\overline{\Delta R} = 0.23$  Å) than for the equatorial donor atoms, especially the oxygen atom ( $\overline{\Delta R} = 0.07$  Å). The average distances in the LS state are 1.90 (Fe–N<sub>eq</sub>), 1.94 (Fe–O<sub>eq</sub>), and 2.02 Å (Fe–N<sub>ax</sub>). A sensible tool for determining the spin state of this type of iron complexes is the O–Fe–O angle, the so-called bite of the ligand. It changes from an average of 108° in the HS state to 90° in the LS state. In Figure 5 a top view of the molecule structures of **1** in the HS and the LS forms is given to illustrate the differences.

(22) Slichter, C. P.; Drickamer, H. G. *J. Chem. Phys.* **1972**, *56*, 2142–2160.

(23) Purcell, K. F.; Edwards, M. P. *Inorg. Chem.* **1984**, *23*, 2620–2625.

(24) (a) McGarvey, J.; Lawthers, I. *J. Chem. Soc., Chem. Commun.* **1982**, 906. (b) Decurtins, S.; Güttlich, P.; Köhler, C. P.; Spiering, H.; Hauser, A. *Chem. Phys. Lett.* **1984**, *105*, 1. (c) Decurtins, S.; Güttlich, P.; Hasselbach, K. M.; Hauser, A.; Spiering, H. *Inorg. Chem.* **1985**, *24*, 2174. (d) Hauser, A. *Chem. Phys. Lett.* **1986**, *124*, 543.

**Table 2.** Selected Bond Lengths [angstroms] and Angles [deg] within the First Coordination Sphere of Octahedral Open-Chain Iron(II) Complexes with Spin State  $S$ 

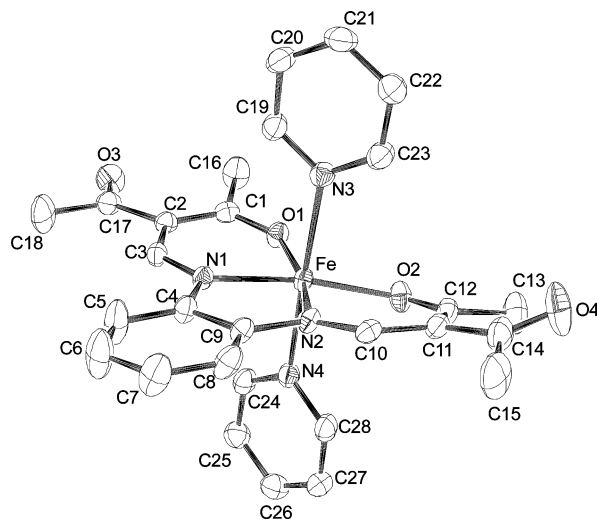
complex	$T$ [K]	$S$	Fe–N1/2	Fe–O1/2	Fe–N3/4	O1–Fe–O2	$N_{ax}$ –Fe– $N_{ax}$	$\angle L1, L2^a$
[FeL(py) <sub>2</sub> ]	200	2	2.061(2) 2.074(1)	1.992(1) 2.009(1)	2.226(2) 2.269(2)	106.99(5)	175.6(1)	16.7
[FeL(py) <sub>2</sub> ]	150	0	1.894(1) 1.906(1)	1.930(1) 1.948(1)	2.007(2) 2.025(2)	89.98(5)	176.1(1)	15.4
[FeL(DMAP) <sub>2</sub> ]	293	2	2.085(4) 2.090(4)	2.008(3) 2.025(3)	2.231(4) 2.272(5)	109.1(2)	171.4(2)	74.6

<sup>a</sup> Angle between the planes of the axial ligands.

**Table 3.** Crystallographic Data for Octahedral Iron(II) Complexes Discussed in This Work

	[FeL(py) <sub>2</sub> ] (HS)	[FeL(py) <sub>2</sub> ] (LS)	[FeL(DMAP) <sub>2</sub> ]
formula	C <sub>28</sub> H <sub>28</sub> N <sub>4</sub> O <sub>4</sub> Fe	C <sub>28</sub> H <sub>28</sub> N <sub>4</sub> O <sub>4</sub> Fe	C <sub>32</sub> H <sub>38</sub> N <sub>6</sub> O <sub>4</sub> Fe
fw, g·mol <sup>-1</sup>	540.39	540.39	636.53
cryst syst	monoclinic	monoclinic	triclinic
space group	$P2_1/c$	$P2_1/c$	$P\bar{1}$
$a$ (Å)	11.9950(8)	11.9910(10)	11.1260(19)
$b$ (Å)	8.8100(5)	8.7183(6)	11.4430(19)
$c$ (Å)	24.9490(15)	24.0105(18)	12.8450(19)
$\alpha$ (deg)	90	90	88.848(19)
$\beta$ (deg)	103.201(7)	101.593(9)	74.890(18)
$\gamma$ (deg)	90	90	80.29(2)
$V$ (Å <sup>3</sup> )	2566.8(3)	2458.7(3)	1555.7(4)
$Z$	4	4	2
$d_{\text{calcd}}$ (g·cm <sup>-3</sup> )	1.398	1.460	1.338
$\mu$ (mm <sup>-1</sup> )	6.29	6.57	5.31
$\Theta$ range, deg	2.13–25.86	2.49–25.79	1.64–24.11
$\lambda$ , Å	0.71073	0.71073	0.71073
$T$ , K	200(2)	150(2)	293(2)
GOF	0.901	0.962	0.665
$R1,^a$ $wR2^b$ ( $I > 2\sigma(I)$ )	0.031, 0.072	0.030, 0.074	0.042, 0.089

<sup>a</sup>  $R1 = \sum |F_o| - |F_c| / \sum |F_o|$ . <sup>b</sup>  $wR2 = [\sum [w(F_o^2 - F_c^2)^2] / \sum w(F_o^2)^2]^{1/2}$ ,  $w = 1/[\sigma^2(F_o^2) + (aP)^2 + bP]$ , where  $P = [F_o^2 + 2(F_c^2)]/3$ .

**Figure 3.** Ortep drawing of **1** in the HS form, showing the 50% probability ellipsoids. Hydrogen atoms have been omitted for clarity.

The expansion of the O–Fe–O angle in the HS state leads to a stronger distortion of the octahedral coordination sphere of the iron center than in the LS state. The orientation of the axial ligands of the pyridine diadduct **1** is nearly coplanar and does not change upon spin transition. The change of the cell volume  $\Delta V/V = 4.3\%$ ,  $\Delta V = 27 \text{ \AA}^3/\text{Fe}$ , is within the region expected for an iron(II) SCO complex ( $\Delta V/V = 3.8\text{--}6\%$ ;  $\Delta V = 25\text{--}35 \text{ \AA}^3/\text{Fe}^1$ ). In contrast to **1**, the orientation of the axial ligands in the DMAP diadduct **2** is staggered.

Selected intermolecular C–C distances, as well as Fe···Fe distances between the molecules involved in these interactions are reported in Table 4 for **1** and Table 5 for **2**. An extract of the molecule packing of **1** and **2** is given in Figures 6 and 7. A close examination of the data reveals that for **1** there are no C–C intermolecular contacts shorter than 3.6 Å (sum of the van der Waals distances for C). Nevertheless a cooperative spin transition takes place. This can be explained if the involved hydrogen atoms of the methyl groups are considered. For those interactions contacts shorter than 4.2 Å (sum of the van der Waals distances for C and H and the distance of C–H bond length) can contribute to cooperative interactions. However, the number of relevant contacts is still very small compared to compound **2**, where the magnetic measurements indicate stronger cooperative interactions during the spin transition. When the temperature decreases from  $\approx 200$  to  $\approx 150$  K, a shortening of the intermolecular distances is observed except for the Fe···Fe' distance. The number of relevant interactions for the cooperativeness of the spin transition does not change. In the case of complex **2** the number as well as the intensity of intermolecular C–C contacts is significantly higher compared to compound **1**. They lead to the formation of a three-dimensional network of strong van der Waals interactions that is responsible for the strong cooperative interactions during the spin transition (Figure 7). The tighter packing of the molecules of **2** compared to compound **1** is also reflected in shorter intermolecular Fe···Fe distances. For the [Fe(L)<sub>2</sub>-(NCS)<sub>2</sub>] family of mononuclear complexes with L = bipy (bipy = 2,2'-bipyridine), phen (phen = 1,10-phenanthroline), and dpp (dpp = dipyrro[3,2-a:2',3'-c]phenazine),<sup>7a</sup> the number and intensity of contacts shorter than the sum of the van der Waals radii is also made responsible for the cooperative nature of the spin transition. However, in contrast to this collection of compounds, this cannot be associated with the aromatic or aliphatic nature of the ligands in our case. The sterically more demanding DMAP ligand obviously supports the closer packing of the molecules. The DMAP methyl groups are involved in most of the close intermolecular C–C contacts. Previously another SCO complex of this family of Schiff-base-like ligands (COOEt instead of COMe as substituents of the equatorial ligand) was published with pyridine as axial ligands.<sup>10,13a</sup> The spin transition of this complex is gradual, and the shortest intermolecular Fe···Fe distance is with 8.9 Å significantly longer than the one found in compound **1**.<sup>13a</sup> Several short intermolecular C–C contacts are found that involve the ethoxy group of the equatorial

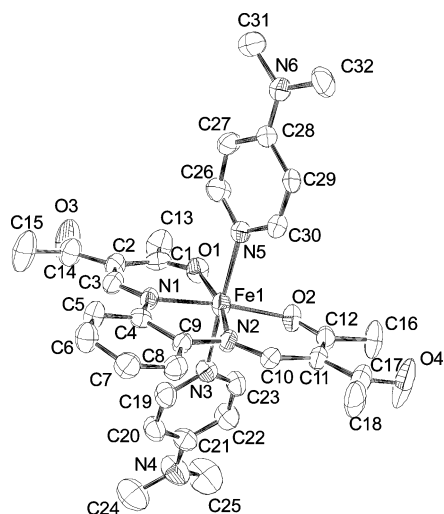


**Figure 4.** Ortep drawing of **2** in the HS form, showing the 50% probability ellipsoids. Hydrogen atoms have been omitted for clarity.

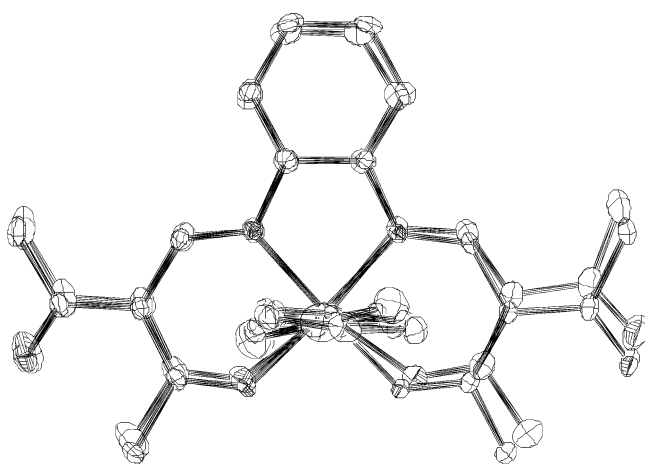


**Figure 5.** Schematic drawing of the top view of both HS and LS forms of **1**. The asymmetric unit at  $T \cong 150$  K is the upper one. Fe–N(1,2) bonds are superimposed. The change in the O–Fe–O angle (HS,  $107^\circ$ ; LS,  $90^\circ$ ) is clearly visible.

substituent. Obviously this group is not suitable (possibly too flexible) for transmitting cooperative interactions during the spin transition in the crystal. The shortest intermolecular Fe $\cdots$ Fe distance appears to be a good indication for the extent of the intermolecular contacts.

**3.3. Optical and Photomagnetic Measurements.** For the two complexes the thermal SCO behavior has been followed by measuring the diffuse absorption spectra (Figures 8–10). When the temperature is cooled from room temperature to 150 K, in both cases the absorption band at around 850 nm, which is a characteristic of the d–d transition of the HS state, decreases. Concomitantly, the absorption bands in the visible range linked to the LS state of both the metal-to-ligand charge-transfer (MLCT) and d–d transitions increase. Figures 8b and 10 report an alternative way to follow the change of the diffuse absorption spectra as function of the temperature by measuring the change of the reflectivity spectra at given selected wavelengths, i.e., 879 and 850 nm (compounds **1** and **2**, respectively). Along the thermal HS  $\rightarrow$  LS spin transition the intensity of the transition band at 879 nm/850 nm decreases, and consequently, the reflectivity signal

**Table 4.** Selected Intermolecular Distances (angstroms) of **1** at 200 K (HS) and 150 K (LS)

	$T \cong 200$ K	$T \cong 150$ K
C21–C16'	4.127	3.916
C16'–C26''	4.007	3.954
Fe $\cdots$ Fe'	8.192	8.190
Fe $\cdots$ Fe''	12.519	12.044
Fe $\cdots$ Fe''	9.726	9.650

**Table 5.** Selected Intermolecular Distances (angstroms) of **2**

C13–C16'	3.866	C5–X18	3.865
C29'–C32''	3.519	C6''–C17'''	3.721
C30'–C32''	3.555	C7''–C10'''	3.555
C31'–C8''	3.778	C7''–C11'''	3.466
C32'–C4''	3.674	C7''–C17'''	3.858
C32'–C5''	3.751	C8''–C10'''	3.365
C32'–C6''	3.931	C8''–C11'''	3.819
C32'–C8''	3.935	C9''–C10'''	3.865
C32'–C9''	3.716		
Fe $\cdots$ Fe'	7.153		
Fe' $\cdots$ Fe''	11.416		
Fe'' $\cdots$ Fe'''	8.108		

increases. But what is interesting to note is that for temperatures below to 50 K, the reflectivity signal of **1** (Figure 8b) oppositely decreases. The same effect is also observable for the complex **2** (Figures 9b, 10); the diffuse absorption spectra recovers the shape and the intensity of 250 K. These observations provide some evidence (i) that at the surface the light-induced LS  $\rightarrow$  HS conversion occurs, according to the LIESST phenomenon,<sup>24</sup> and (ii) that the lifetime of the photoinduced HS state below 50 K is sufficiently long to allow the optical excitation by a halogen light source delivering around  $5 \text{ mW}\cdot\text{cm}^2$ .

The diffuse absorption spectra of **1** and **2** (Figures 8a and 9) have also evidenced that signals in the visible range are close to the unity (i.e., saturation), in agreement the observable dark color. That can have some strong consequences to quantitatively induce light excitation into bulk condition, like by using a SQUID magnetometer. If the opacity of the sample is important, the light penetration can be prevented and the photoexcitation appears incomplete. The sample can be described as biphased with a top phase at the surface saturated in terms of photoexcitation and a bottom phase practically unexcited. From the results given by the reflectivity analysis of **1** (Figure 8b) even at the surface the photoexcitation level is far to be quantitative. Only 20% of the molecules appear to be photoconverted. At the opposite the almost similar diffuse absorption spectra recorded for **2** at 10 and 250 K suggest that the level of photoexcitation at the surface is close to be quantitative. This is confirmed by the results from the reflectivity analysis (Figure 10). As a consequence of all that we have decided to only perform the photomagnetic investigation (i.e., in bulk condition) on sample **2**. Several tests have been done in order to map the effect of the different wavelengths.

The first irradiation was performed by using a laser red light emitting at 647.1–676.4 nm. After that we have tried to increase the photoexcitation by irradiating with (i) a photodiode-generated IR beam ( $\lambda = 830$  nm) and (ii) a laser green light ( $\lambda = 530.9$  nm). In both cases the photoexcitation was lower than the one obtained with 647.1–676.4 nm

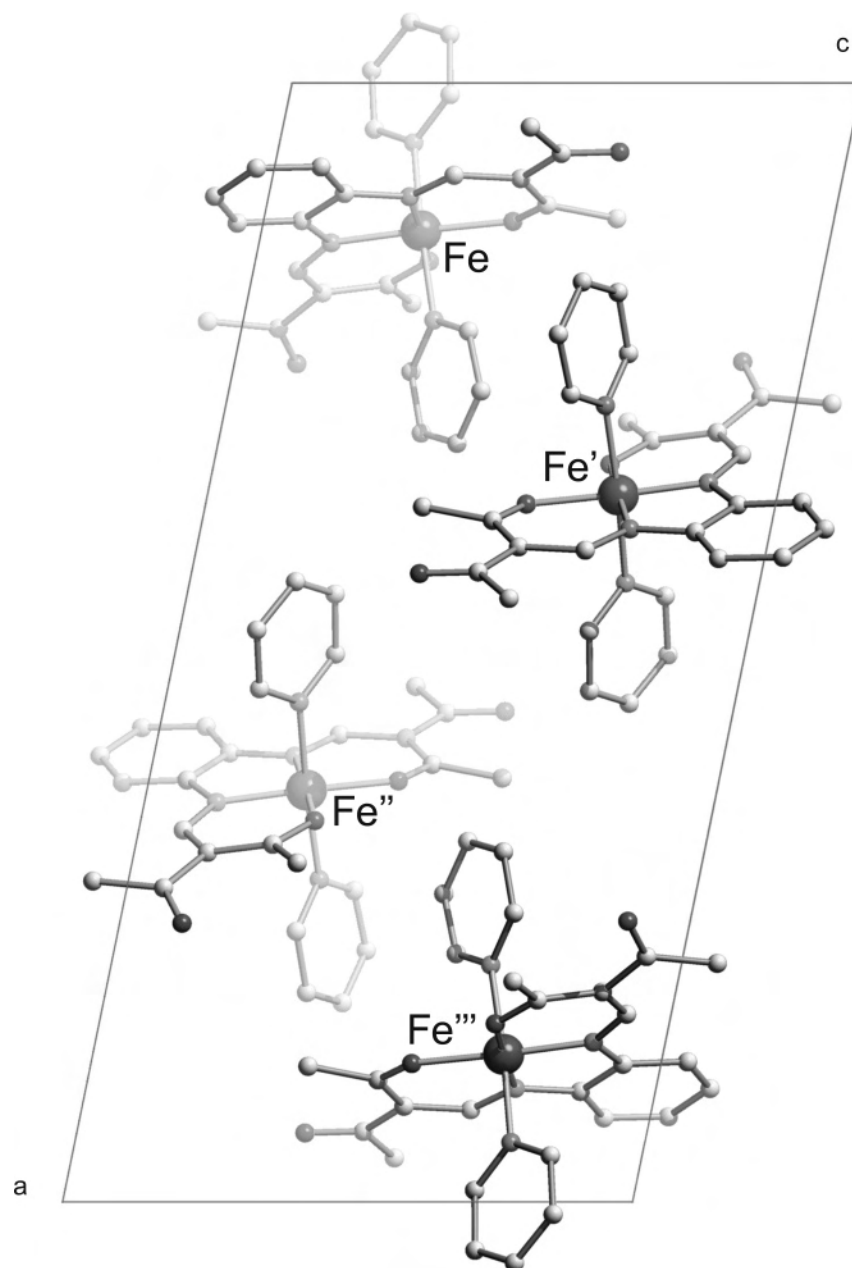


**Figure 6.** Projection of the molecular structure of **1** in HS state along the  $b$ -axis.

wavelengths. Nevertheless a distinct photoexcitation at  $\lambda = 752.5\text{--}799.3$  nm has allowed us to improve the level of photoinduced HS state up to 60% (40% for irradiation at 647.1–676.4 nm). The plots of  $T(\text{LIESST})$  experiments performed by irradiating both at 647.1–676.4 nm and at 752.5–799.3 nm are reported in Figure 11. In this procedure, the irradiation was maintained until complete saturation of the signal, then the light was switched off, and the temperature slightly increased at  $0.3\text{ K min}^{-1}$ . The minimum of the  $d\chi_M T/dT$  versus  $T$  curve defines the  $T(\text{LIESST})$  limit temperature (i.e., 53 K for **2**) above which the light-induced magnetic HS information is erased in a SQUID cavity.<sup>9,25</sup> The decrease of the  $\chi_M T$  product of the light-induced HS state at low temperatures can be attributed to zero-field splitting effects.<sup>17b,c</sup>

Additionally we performed kinetic studies of **2** from 10 K to the highest temperatures compatible with our SQUID setup, that is typically close to the  $T(\text{LIESST})$  values. The profiles of the different kinetics are shown in Figure 12. The most striking feature of these relaxation curves is the strong deviation from single exponential, and a marked sigmoidal law can be applied in agreement with a self-accelerated behavior predicted for strong cooperative systems.<sup>26,27</sup> In that

(25) (a) Létard, J.-F.; Capes, L.; Chastanet, G.; Moliner, N.; Létard, S.; Real, J. A.; Kahn, O. *Chem. Phys. Lett.* **1999**, *313*, 115. (b) Marcen, S.; Lecren, L.; Capes, L.; Goodwin, H. A.; Létard, J.-F. *Chem. Phys. Lett.* **2002**, *358*, 87. (c) Létard, J.-F.; Guionneau, P.; Nguyen, O.; Costa, J. S.; Marcén, S.; Chastanet, G.; Marchivie, M.; Capes, L. *Chem. Eur. J.* **2005**, *11*, 4582. (d) Carbonera, C.; Costa, J. S.; Money, V. A.; Elhak, J.; Howard, J. A. K.; Halcrow M. A.; Létard, J.-F. *Dalton Trans.* **2006**, 3058.

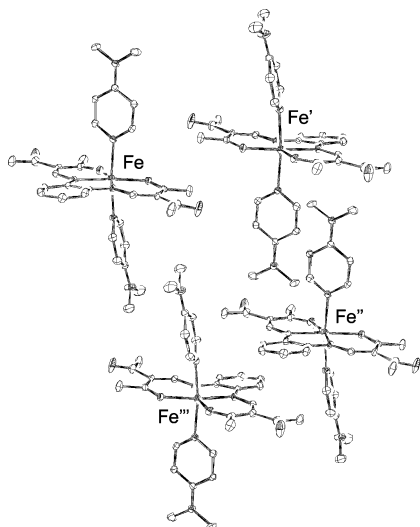


Figure 7. Molecule packing of **2** in HS state.

case the height of the energy barrier is an increase (or a decrease) function of  $\gamma_{\text{HS}}$  (or  $\gamma_{\text{LS}}$ ) and the relaxation rate  $k_{\text{HL}}^*(T, \gamma_{\text{HS}})$  depends exponentially on both  $\gamma_{\text{HS}}$  and  $T$  (eqs 2 and 3) with  $\alpha(T)$  ( $= E_a^*/k_{\text{B}}T$ ) the acceleration factor at a given temperature (eq 3).

$$\frac{\partial \gamma_{\text{HS}}}{\partial t} = -k_{\text{HL}}^* \gamma_{\text{HS}} \quad (2)$$

$$k_{\text{HL}}^*(T, \gamma_{\text{HS}}) = k_{\text{HL}}(T) \exp[\alpha(T)(1 - \gamma_{\text{HS}})] \quad (3)$$

The least-squares fit of our data have been performed with a sigmoidal model where  $k_{\text{HL}}(T)$  and  $\alpha(T)$  are refined as free parameters. The calculated curves are shown as solid lines in Figure 12, and the parameters are listed in Table 6. The apparent activation energy,  $E_a = 550 \text{ cm}^{-1}$ , and the apparent pre-exponential factor,  $k_{\infty} = 5.5 \times 10^2 \text{ s}^{-1}$ , of the activated region are calculated from the straight line given by the  $\ln k_{\text{HL}}(T)$  versus  $1/T$  plot in the 45–52 K range. Hauser and co-workers have evidenced a mathematical relation (eq 4) between the acceleration factor  $\alpha(T)$  recorded at low temperatures and the cooperativity parameter  $\Gamma$  of the thermally activated region where the initial reduced energy gap  $n_0$  is small.<sup>26,27</sup> With the use of the experimental value  $\alpha(T) = 7$  estimated at 52 K, a predicted  $\Gamma$  value of around  $240 \text{ cm}^{-1}$  is expected, somewhat reasonable in regard to the  $315 \text{ cm}^{-1}$  ( $\Gamma = 3.78 \text{ kJ/mol}^{-1}$ ) derived in the thermal SCO regime.

$$\alpha(T) = \Gamma/k_{\text{B}}T \quad (4)$$

An elegant way to test the validity of all the kinetics parameters, which have been recorded in a small window of temperatures (45–52 K) imposed by the use of a SQUID magnetometer, is to reproduce the experimental  $T(\text{LIESST})$

curve.<sup>17b,c</sup> For that it is necessary to carefully take into account the time and the temperature dependencies. In a measurement of a  $T(\text{LIESST})$  curve, the sample was first irradiated at 10 K, then without further irradiation the temperature was slowly warmed at the rate of approximately  $0.3 \text{ K min}^{-1}$ . Rigorously, the temperature during a  $T(\text{LIESST})$  measurement, in a SQUID cavity, is changed in 1 K steps. At each temperature  $T_i$ , the time for the signal acquisition is 60 s and the time to reach the next temperature is 120 s. In reality, it is difficult to reproduce the relaxation connected to the stabilization of the temperature. In a first approximation, we have decided to neglect this subtle effect and the relaxation is calculated at each temperature  $T_i$  during the global time of 180 s. The  $\gamma_{\text{HS}}$  fraction obtained after 180 s of relaxation at  $T_i$  is used as started value for the next temperature,  $T_{i+1}$ , i.e.,  $(\gamma_{\text{HS}})_{t=180}^{T=T_i} = (\gamma_{\text{HS}})_{t=0}^{T=T_{i+1}}$ .

Another important point in the simulation of the  $T(\text{LIESST})$  curve is that such an experiment combines the relaxation of both the tunneling and the thermally activated regions. Rigorously, this imposes us to use the theory of the nonadiabatic multiphonon process in the strong vibronic coupling limit.<sup>28</sup> In a first approximation, we have assumed that the evolution of the HS fraction is just a summation of the two effects.<sup>17b,c</sup> For a cooperative compound exhibiting sigmoidal relaxation curves, as encountered, eq 5 can be used.

$$\left(\frac{\partial \gamma_{\text{HS}}}{\partial t}\right)_{T_i} = -\gamma_{\text{HS}} \{k_{\text{HL}}(T \rightarrow 0) + k_{\infty} \exp(-E_a/k_{\text{B}}T_i)\} \exp[\alpha(T_i)(1 - \gamma_{\text{HS}})] \quad (5)$$

For a mononuclear SCO complex, the  $T(\text{LIESST})$  curve is finally calculated by taking into account the anisotropy of the HS iron(II) ion in an octahedral surrounding. This phenomenon called zero-field splitting is associated to the spin-orbit coupling between the ground state and the excited state in a zero applied magnetic field. For an iron(II) ion in HS configuration, the  $S = 2$  ground state is split into three levels. The magnetic contribution of each state is determined by their energy separation,  $D$ , and their thermal population.<sup>29</sup> For a powder sample, the  $(\chi_{\text{M}}T)_{\text{ZFS}}$  product associated to the zero-field splitting and the  $\chi_{\text{M}}T$  of the  $T(\text{LIESST})$  curve are, respectively, given by eqs 6 and 7,

$$(\chi_{\text{M}}T_i)_{\text{ZFS}} = \frac{\chi_{\text{M}}T_{i\parallel} + 2\chi_{\text{M}}T_{i\perp}}{3} \quad (6)$$

$$\text{with } \chi_{\text{M}}T_{i\parallel} = \frac{3g^2}{4} \frac{e^{-D/k_{\text{B}}T_i} + 4e^{-4D/k_{\text{B}}T_i}}{1 + 2e^{-D/k_{\text{B}}T_i} + 2e^{-4D/k_{\text{B}}T_i}}$$

$$\text{and } \chi_{\text{M}}T_{i\perp} = \frac{1}{4} \frac{g^2 k_{\text{B}}T_i}{D} \frac{9 - 7e^{-D/k_{\text{B}}T_i} - 2e^{-4D/k_{\text{B}}T_i}}{1 + 2e^{-D/k_{\text{B}}T_i} + 2e^{-4D/k_{\text{B}}T_i}}$$

$$\chi_{\text{M}}T_i = (\chi_{\text{M}}T_i)_{\text{ZFS}} \gamma_{\text{HS}}(t, T_i) \quad (7)$$

(26) Hauser, A. *Spin Crossover in Transition Metal Compounds*; Gülich, P., Goodwin, H. A., Eds.; Topics in Current Chemistry; Springer: Wien, New York, 2004; Vol. 234, p 155.

(27) (a) Hauser, A. *Coord. Chem. Rev.* **1991**, *111*, 275. (b) Hauser, A.; Jetic, J.; Romstedt, H.; Hinek, R.; Spiering, H. *Coord. Chem. Rev.* **1999**, *471*, 190–192.

(28) Buhks, E.; Navon, G.; Bixon, M.; Jortner, J. *J. Am. Chem. Soc.* **1980**, *102*, 2918.

(29) Kahn, O. *Molecular Magnetism*; VCH: New York, 1993.

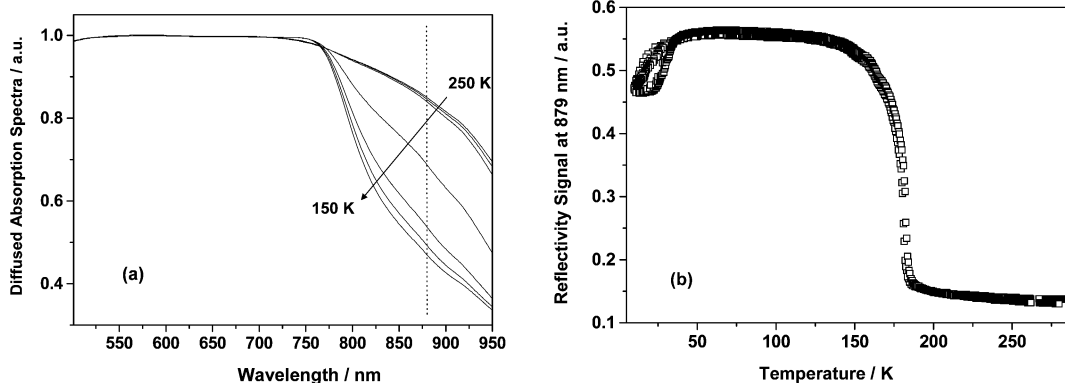


**Figure 8.** Dependency of the diffuse absorption spectra (a) and of the reflectivity signal at 879 nm (b) for **1** as function of both temperature and light irradiation.

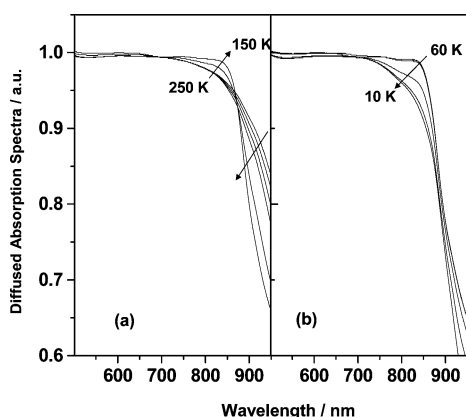


**Figure 9.** Dependency of the diffuse absorption spectra of **2** as function of both temperature and light irradiation with (a) the thermal spin crossover (SCO) and (b) the light-induced regions.

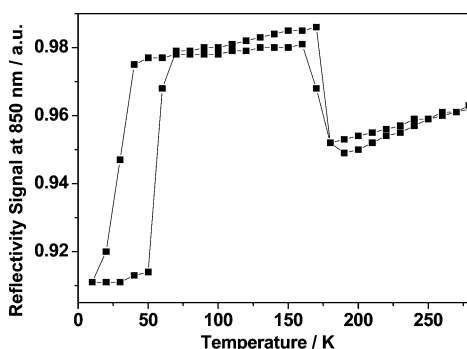


**Figure 10.** Dependency of the reflectivity signal at 850 nm for **2** as function of both temperature and light irradiation.

The main difficulty of this simulation is consequently to satisfactorily estimate the rate constant  $k_{HL}(T \rightarrow 0)$  of the tunneling region. In the present work, we have considered in first hypothesis that the last complete kinetic measurement recorded at low temperature (i.e., 43 K) could be regarded as an upper limit of the  $k_{HL}(T \rightarrow 0)$  value (Table 6). On the basis of this and by using the deduced  $E_a$ ,  $k_{\infty}$ , and  $\alpha(T)$  parameters, the agreement found between the calculated and the experimental  $T(\text{LIESST})$  curves was very good (Figure 11).

Another way to see the effect of the cooperativity on the photoexcitation and relaxation process is to monitor the

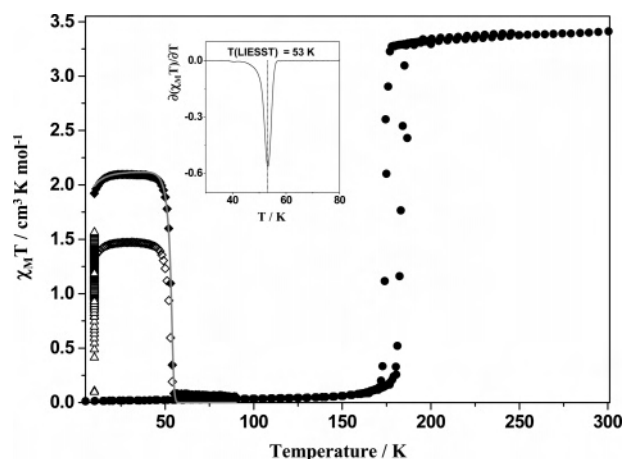


**Figure 11.** Temperature dependence of  $\chi_M T$  for **2**. ● = data recorded in the cooling and warming mode without irradiation; △ = data recorded with irradiation at 10 K; ◆ =  $T(\text{LIESST})$  measurement, data recorded in the warming mode with the laser turned off after irradiation for 1 h at 752.5–799.3 nm (◇ = at 647.1–676.4 nm). The solid line through the  $T(\text{LIESST})$  measurement shows the fit generated from the deduced experimental thermodynamic parameters. The inset figure reports the region where the minimum of the derivate  $d\chi_M T/dT$  curve gave the  $T(\text{LIESST})$  temperature.

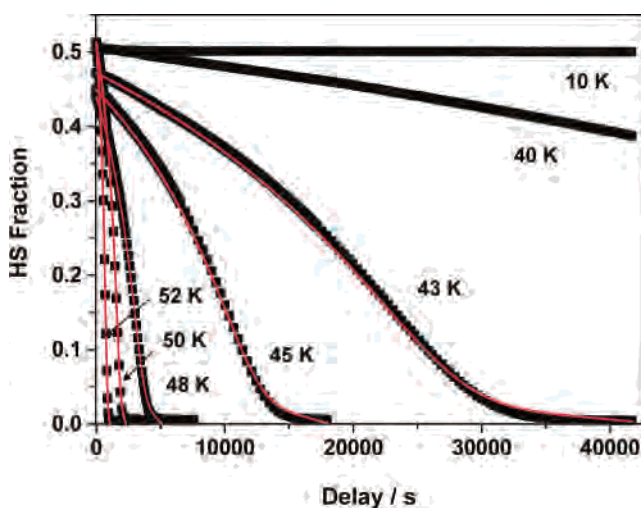


**Figure 12.** Kinetics studies of **2** as function the temperature. The photoexcitation was generated at 10 K with at krypton laser source (647.1–676.4 nm).

magnetic properties of a SCO material under constant irradiation. The competition between the constant photo-

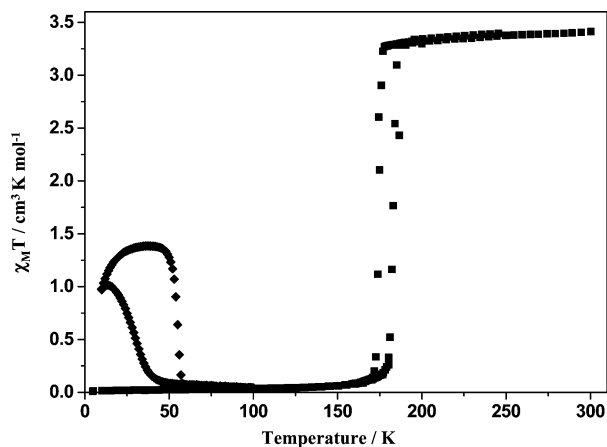


**Figure 13.** LITH experiments, the temperature dependence of  $\chi_M T$  recorded in the warming and cooling modes with irradiation.

**Table 6.** Kinetics Parameters Governing the Photoinduced HS  $\rightarrow$  LS Relaxation of **2** as Function of the Temperature

$T/K$	43	45	48	50	52
$k_{HL}(T)/s^{-1}$	$7.9 \times 10^{-7}$	$1.1 \times 10^{-6}$	$2.6 \times 10^{-6}$	$7.5 \times 10^{-6}$	$1.6 \times 10^{-5}$
$\alpha(T)$	6.5	7	7	7	7

excitation and the self-accelerated thermal relaxation process is well-known to induce in the region of  $T(\text{LIESST})$  a thermal hysteresis loop, named LITH (light-induced thermal hysteresis).<sup>17a,30</sup> Figure 13 shows the LITH loops observed for **2** under constant irradiation. All that once more proves that the light-induced HS phase of **2** is also strongly cooperative.

#### 4. Concluding Remarks

The synthesis and characterization of two new SCO complexes with a 2 and 9 K wide, respectively, hysteresis have been reported. Results from X-ray structure analysis indicate that the number and intensity of close intermolecular contacts is responsible for cooperative nature of the spin transition. The wider hysteresis in the case of compound **2** appears to be due to the bulkier DMAP ligand. The methyl groups of this ligand are involved in plenty of the close intermolecular C–C contacts. The greater number of intense intermolecular C–C contacts is also reflected in shorter intermolecular Fe $\cdots$ Fe distances in **2** compared to **1**.

Concerning the investigations of the LIESST properties, we have first performed a diffuse reflectivity study. We have noticed that for the compound **1** at the surface the level of photoconversion was less than 20%. In contrast compound **2** displays almost quantitative photoexcitation (Figures 8 and 10). Very often such an effect reflects a higher  $T_{1/2}$ , in regard to the inverse energy gap law introduced by Hauser and co-workers<sup>27</sup> or the  $T(\text{LIESST})$  versus  $T_{1/2}$  relation of Létard and co-workers.<sup>17,25</sup> But here the difference between the  $T_{1/2}$  values of **1** and **2** is not really significant. The explanation deals with the optical data. Compound **2** benefits from a bleaching effect in the range of 700–850 nm that is below an isosbestic point located at around 880 nm. Compound **1** exhibits similar features but located at smaller wavelengths and close to the saturation. In other words at 752.5–799.3 nm in the LS state compound **2** displays a stronger absorption band than **1**.

(30) Desaix, A.; Roubeau, O.; Jeftic, J.; Haasnoot, J. G.; Boukheddaden, K.; Codjovi, E.; Linares, J.; Nogues, M.; Varret, F. *Eur. Phys. J. B* **1998**, *6*, 183.

Concerning now the fact that under irradiation at 752.5–799.3 nm a direct LIESST process occurs for compound **2**, this differs from the reverse-LIESST effect well-known for tetrazole derivatives. In fact, this behavior can be understood by the presence of an intense <sup>1</sup>MLCT–LS electronic transition into the visible range which partially masks the d–d transition of the HS state even at 800–850 nm. Similar behavior has been also described for the phase I of the [Fe-(PM-BiA)<sub>2</sub>(NCS)<sub>2</sub>] complex *cis*-bis(thiocyanato)-bis[(*N*-2'-pyridylmethylene)-4(aminobiphenyl)] iron(II).<sup>17a,b</sup> The irradiation on the borderline of the <sup>1</sup>MLCT–LS absorption is able to induce the population of the metastable HS state through the direct LIESST process.

One further aim in studying the LIESST effect is to achieve  $T(\text{LIESST})$  values close to room temperature toward attaining materials which can act as light-initiated molecular switches.<sup>17c</sup> Along that the systematic investigation of the LIESST properties of more than 60 iron(II) SCO materials have suggested the existence of a relationship between the  $T(\text{LIESST})$  and the  $T_{1/2}$  values, such as  $T(\text{LIESST}) = T_0 - 0.3T_{1/2}$ .<sup>17,25</sup> These studies reveal four distinct  $T_0$  lines dependent on the geometry and rigidity of ligands around the iron(II) center; 100 K for monodentate ligands,<sup>25a</sup> 120 K for bidentate ligands,<sup>25a</sup> 150 K for meridional tridentate ligands,<sup>25b,c</sup> and 200 K for three-dimensional network solids.<sup>31</sup> Following this trend complexes **1** and **2**, involving tetradentate ligands, are potentially interesting. But the photomagnetic study performed on **2**, in regard to the  $T_{1/2}/T(\text{LIESST})$  couple, is disappointing and obeys to the  $T_0 = 100$  K line like the properties predicted for an iron(II) complex bearing a monodentate ligand. This result is consistent with the recent observation done for SCO complexes with tridentate ligands possessing some degree of freedom carried by unsaturated carbon atom between the aromatic rings, where the  $T(\text{LIESST})$  values also follow the  $T_0 = 100$  K line.<sup>32</sup> This emphasizes the concept that vibrational aspects and hardness of the inner coordination sphere are the key factors for stabilizing the metastability of the light-induced HS state.<sup>17c,32a</sup> Thus, the observations found here for complex **2**, where the tetradentate L ligand possesses flexible unsaturated nitrogen atoms connecting the aromatic phenyl rings, show that it is a new example of a nonoptimized ligand system in regard to the stabilization of the light-induced HS state.

**Acknowledgment.** This work has been supported financially by the Deutsche Forschungsgemeinschaft (SPP 1137) and the Fonds der Chemischen Industrie. The authors also thank the Aquitaine Region for funding the Photomagnetic platform at the ICMCB.

**Supporting Information Available:** Crystallographic and Mössbauer data. This material is available free of charge via the Internet at <http://pubs.acs.org>.

IC0700670

- (31) Shimamoto, N.; Ohkoshi, S.-S.; Sato, O.; Hashimoto, K. *Inorg. Chem.* **2002**, *41*, 678.
- (32) (a) Bonhommeau, S.; Brefuel, N.; Pálfi, V. K.; Malnár, G.; Zwick, A.; Salmon, L.; Tuchagues, J.-P.; Costa, J. S.; Létard, J.-F.; Paulsen, H.; Bousseksou, A. *Phys. Chem. Chem. Phys.* **2005**, *7*, 2909. (b) Enachescu, C.; Linares, J.; Varret, F.; Boukheddaden, K.; Codjovi, E.; Salunke, S. G.; Mukherjee, R. *Inorg. Chem.* **2004**, *43*, 4880. (c) Leita, B.; Neville, S.; Halder, G.; Moubarakhi, B.; Kepert, C.; Létard, J.-F.; Murray, K. *Inorg. Chem.* **2007**, *46*, 8784.